Physica E 120 (2020) 114118

Contents lists available at ScienceDirect

Physica E: Low-dimensional Systems and Nanostructures

journal homepage: www.elsevier.com/locate/physe

Controlling anisotropic surface group velocity and effective mass in topological crystalline insulator SnTe by Rashba effect

Khang D. Pham [a,b], Nguyen T.T. Binh [c,*], Ho Viet [d], Nguyen T. Dung [e], Bui D. Hoi [f,*]

[a] Laboratory of Applied Physics, Advanced Institute of Materials Science, Ton Duc Thang University, Ho Chi Minh City, Viet Nam
[b] Faculty of Applied Sciences, Ton Duc Thang University, Ho Chi Minh City, Viet Nam
[c] Institute of Research and Development, Duy Tan University, Danang 550000, Viet Nam
[d] Department of Research Management and International Relations, Hue Industrial College, Hue City, Viet Nam
[e] Vinh University, Nghe An Province, Viet Nam
[f] Department of Physics, University of Education, Hue University, 34 Le Loi, Hue City, Viet Nam

ABSTRACT

Rashba effect has become important in the realization of exotic topological features. Herein, we theoretically investigate the Rashba spin–orbit coupling (RSOC) effects on the dispersion energy, group velocity (GV) and effective mass (EM) of Dirac fermions in the topological crystalline insulator SnTe (001) surface. We found that different classes of RSOCs do not change the qualitative behavior of the band structure; its main effect is to break the symmetry of the gapless bands down to a group of discrete rotations and to slightly shift the phase boundaries. Moreover, the inherent anisotropic surface features hold with RSOC. The modulation mechanism of RSOC effects is further analyzed from the orientation-dependent GV and EM at different RSOC values. It is found that the GV and EM of fermions are band-dependent and symmetric concerning the RSOC sign, which plays a decisive role in modifying the optical properties. Our study provides new insight into the designing nanodevices for electric-field-controllable topological electronics.

1. Introduction

The recent discovery of gapless critical phases in novel quantum materials, so-called topological insulators (TIs) has revived interest both theoretically and experimentally in the band topology of insulators [1–10]. The first gapless states in 2D materials have been observed in graphene [pristine state], silicene and related group-IV materials [in the presence of electric field equal to the intrinsic spin–orbit coupling], etc [11–22]. In 2011, Fu [23] extended the topological classification of band structures to include certain spatial symmetries in addition to the time-reversal symmetry, particle–hole symmetry and chiral symmetry in TIs [1–4,24,25]. The new class is called topological crystalline insulators (TCIs), which have metallic surface states with quadratic band degeneracy on high symmetry crystal surfaces. An insulating bulk and metallic surface states determine the novel topological features in both TCIs and TIs.

The comparison between TIs and TCIs shows that a common TI supports an odd number of metallic surface states, while a TCI has an even number of surface states. On the other hand, TI surface states are robust enough against the external perturbations, while TCI metallic surface states can be tuned easily by various types of perturbations [26], implying that the physical features of TCI can be easily controlled. The first search for fascinating features of TCIs in real materials was measurable in experimental observations by angle-resolved photoemission spectroscopy (ARPES), which reported a lead thin salt family in IV-VI semiconductors mainly SnTe, $Pb_{1-x}Sn_xSe$ ($x \geq 0.2$) and $Pb_{1-x}Sn_xTe$ ($x \geq 0.4$) [27–29]. Reflection symmetry is the origin of the non-trivial topology of electronic bands in these TCIs [27–31]. However, reduction of spatial crystal symmetry is in challenge [27,32–39].

Recently, much attention has been focused on the effect of the Rashba spin–orbit coupling (RSOC) in low-dimensional topological and non-topological materials [40–44], which it has been established that the RSOC can be controlled through a gate voltage [45–48]. By this, in turn, one can control the band gap externally by applying an electric field. The Rashba induced effects by the gate voltage or electric field act as mirror symmetry breaking terms. As a result of this crystal symmetry breaking, the edge states disappear in the presence of the external Rashba effect, introducing a topological transistor with tunable ON and OFF states [37]. Although there are two types of metallic gapless states in TCIs, (111) and {(110), (001)} surface states, we are interested in the (001) one, since it has been observed experimentally a lot as well as confirmed theoretically [49–60]. On the $SnTe/Pb_{1-x}Sn_xSe/Pb_{1-x}Sn_xTe$ (001) surface states, four robust Dirac cones are centered at mirror-symmetry-invariant X and Y points [28–30,49,61,62].

Thus, IV–VI semiconductors are extremely versatile platforms for novel topological device applications, however; the investigation of fundamental physical properties of Dirac fermions on the SnTe (001)

* Corresponding authors.
E-mail addresses: phamdinhkhang@tdtu.edu.vn (K.D. Pham), nguyentthanhbinh8@duytan.edu.vn (N.T.T. Binh), buidinhhoi@hueuni.edu.vn (B.D. Hoi).

https://doi.org/10.1016/j.physe.2020.114118
Received 8 February 2020; Received in revised form 14 March 2020; Accepted 23 March 2020
Available online 26 March 2020

surface in the presence of RSOC is still of great interest. In this paper, we study the group velocity and effective mass quantities, in which the Rashba effects on their evolution have not been reported well theoretically to date. Since both the electronic properties of semiconductors and thermoelectrics, in particular, are typically understood using band models, transport is then understood in terms of band expressions with a varying group velocity and effective mass. For this reason, it is expected to have new physical insights when the Rashba effects are considered in real transport. One may ask that why RSOC? The answer can be understood from the fact that the magnetic field and the exchange field are hard to control precisely, while a precise control of the electric field is possible within current techniques [43,44].

The rest of the paper is organized as follows. In Section 2, we review the effective $\vec{k}\cdot\vec{p}$ Hamiltonian model of SnTe (001) surface states for the momenta projected to the surface BZ (SBZ) in the absence and presence of RSOC. Two-dimensional (2D) and three-dimensional (3D) band structures are also printed in this section to discuss the alterations of RSOC-dependent bands. The "Rashba-induced" group velocity (GV) and effective mass (EM) calculations are presented in Sections 3 and 4. We use the traditional semi-classical approach by associating particles with wave-packets to calculate these transport properties. In Section 5 the paper is summarized.

2. Theory

2.1. Model Hamiltonian

The surface states of the SnTe (001) TCI and related alloys around the X and Y point can be described by the effective 2D Hamiltonian, respectively, [28–30]

$$\hat{\mathcal{H}}_X^0(\vec{k}) = \eta_1 k_x\hat{\sigma}_y - \eta_2 k_y\hat{\sigma}_x + n\hat{\tau}_x + \delta\hat{\sigma}_y\hat{\tau}_y\,, \tag{1a}$$

$$\hat{\mathcal{H}}_Y^0(\vec{k}) = \eta_2 k_x\hat{\sigma}_y - \eta_1 k_y\hat{\sigma}_x + n\hat{\tau}_x + \delta\hat{\sigma}_x\hat{\tau}_y\,, \tag{1b}$$

where $\hat{\vec{\sigma}} = (\hat{\sigma}_x, \hat{\sigma}_y)$ and $\hat{\vec{\tau}} = (\hat{\tau}_x, \hat{\tau}_y)$ are the Pauli matrices in spin and surface space (pseudospin describing the cation–anion degree of freedom), respectively, $\eta_1 = 1.3$ eV Å and $\eta_2 = 2.4$ eV Å are typical values obtained from numerical *ab initio* computations [27,49,63], and two parameters $n = 70$ meV and $\delta = 26$ meV are the intervalley scattering at the lattice scale [27]. We have set the physical constant $\hbar = 1$ for simplicity. Note that the model is the same for SnTe (001) surface and related alloys, not all IV-VI semiconductors. However, the Fermi velocities η_1 and η_2 are not the same in all of the alloys and should be fitted numerically to the experimental or DFT theoretical works on each compound.

Using the replacements $\hat{\sigma}_x \mapsto \hat{\sigma}_y$, $\hat{\sigma}_y \mapsto -\hat{\sigma}_x$, $k_x \mapsto k_y$, and $k_y \mapsto -k_x$ in Eq. (1a), Eq. (1b) can be obtained. This reminds the four-fold C_4 discrete rotation symmetry and allows us to focus on one of them only. Here, we will consider X point. As well-known, via diagonalizing the Hamiltonian in Eq. (1a), the direction-dependent dispersion energy relation of four gapless surface states can be easily obtained as

$$\mathcal{E}_X^{0^{\mu,\nu}}(\vec{k}) = \mu\sqrt{\mathcal{P}^2 + \eta_1^2k_x^2 + \eta_2^2k_y^2 + 2\nu\sqrt{\mathcal{P}^2\eta_1^2k_x^2 + n^2\eta_2^2k_y^2}}\,, \tag{2}$$

where $\mathcal{P}^2 = n^2 + \delta^2$ is the reduced intervalley scattering parameter. $\mu = +(-)$ and $\nu = +(-)$ refer to the conduction (valence) band and Dirac point Λ_x (Λ_x') point, respectively.

A schematic contour plot of the SBZ for different Fermi surface energies is depicted in Fig. 1. In this figure, the horizontal and vertical dashed line shows the wave-vectors k_x and k_y, respectively, which are tunable parameters of the system. Consider the right panel for wave pockets around the X point. At $k_x = k_y = 0$ coordinate, i.e. exactly the position of X point, fermions have the energies $\mathcal{E} = \pm\mathcal{P}$, while at $\mathcal{E} = 0$, the points $\Lambda_x = (+\mathcal{P}/\eta_1, 0)$ and $\Lambda_x' = (-\mathcal{P}/\eta_1, 0)$ appear, i.e. two Dirac points characterizing the metallic gapless SnTe (001) surface states. In addition to these points, at $k_x = 0$, two saddle points $S_1 = (0, +n/\eta_2)$ and $S_2 = (0, -n/\eta_2)$ along the y direction are appeared. Moreover, the touched orange colors show the criteria that two disconnected electronic wave pockets suffer from a Fermi surface shape change, so-called the Lifshitz transition [a change in the topology of a Fermi surface, which involve the appearance of zeros in the energy spectrum of a many-body fermion system, excluding the normal Fermi surface, of course] at energy $\mathcal{E} = \pm\delta = \pm 26$ meV. For the contribution of bands to these spatial distributions, one can look at the band dispersions directly.

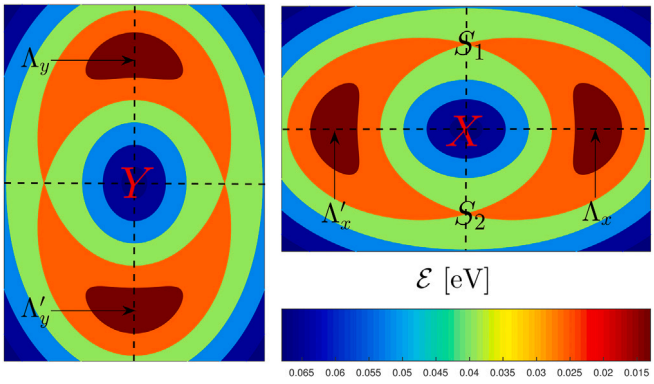

Fig. 1. (Color online) Bounded isoenergy SBZs by the X/Y points. Low-energy Dirac cones, i.e. metallic gapless SnTe (001) surface states, are located at $\{\Lambda_x, \Lambda_x'\}$ and $\{\Lambda_y, \Lambda_y'\}$ points near the X and Y point, respectively. The horizontal (vertical) dashed line shows the wave-vector k_x (k_y). Two disconnected electron pockets at low-energy suffer from a Lifshitz transition at energy $\mathcal{E} = \pm\delta = \pm 26$ meV, leading to two saddle points S_1 and S_2.

2.2. Rashba spin–orbit coupling effects on the dispersion energy of Dirac fermions on the SnTe (001) surface

In this subsection, we introduce the RSOC Hamiltonian. Experimentally, RSOC is inevitably introduced by gating. By considering the RSOC term on the SnTe (001) surfaces, the Hamiltonian around the X point is modified to

$$\hat{\mathcal{H}}_X(\vec{k}) = \hat{\mathcal{H}}_X^0(\vec{k}) + \hat{\mathcal{H}}_{\rm RSOC}(\vec{k})\,, \tag{3}$$

The result of a combination of spin–orbit interaction and asymmetry of the crystal is a momentum-dependent splitting of spin bands and an inversion symmetry breaking perpendicular to the SnTe (001) surface [64]. The RSOC term in the momentum space is given by [43,44]

$$\hat{\mathcal{H}}_{\rm RSOC}(\vec{k}) = \mathrm{i}\sum_l \lambda_l \sum_{n=1}^{N_l} \vec{\sigma}\cdot\vec{d}_n^{\,l} e^{\mathrm{i}\vec{d}_n^{\,l}\cdot\vec{k}}\,, \tag{4}$$

where $\vec{d}_n^{\,l} = |\vec{d}_n^{\,l}|(\cos n\pi/2, \sin n\pi/2)$ connects a pair of the lth-nearest neighbor sites (between N_l ones) in the real space and λ_l stands for the corresponding RSOC strengths. The rotation angle $n\pi/2$ is restricted to the four-fold crystal group of the SnTe (001) surface symmetry. Since the SnTe (001) surface is a squared lattice, we take the contributions of the nearest-neighbor ($l = 1$) and next-nearest-neighbor ($l = 2$) sites into account only. The coupling strengths λ_1 and λ_2 tune the quantum phase of SnTe (001) surface states such as band gap opening [43,44,65,66]. By inserting this RSOC Hamiltonian into the Eq. (1a), in the vicinity of X point, the full model Hamiltonian of the present work can be obtained. The best advantage of this RSOC model is that it can be easily expanded to a triangular lattice with the C_6 symmetry or even a square lattice with the C_2 symmetry.

Diagonalizing the RSOC-induced Hamiltonian results in the RSOC-induced direction-dependent dispersion energy. We consider two cases (i) $\lambda_2 = \lambda_1$ and (ii) $\lambda_2 = -2\lambda_1$. Note that we considered all possible configurations of these two RSOCs, but these two are the cases that show almost the same behaviors as other cases. For this reason, we

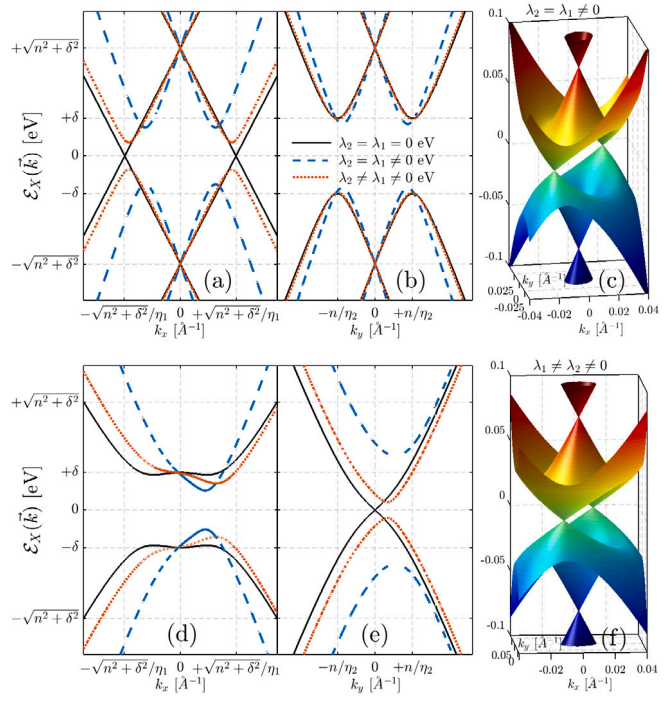

Fig. 2. (Color online) Schematic figure shows the dispersion of Dirac fermions on the SnTe (001) surface near the X point in the absence and presence of RSOC ($\lambda_2 = \lambda_1 = 0.75$ eV and $\lambda_2 = -2\lambda_1 = 1.0$ eV) for (a) $k_y = 0$, (b) $k_x = 0$, (c) 3D band structure for $\lambda_2 = \lambda_1 = 0.75$ eV along both x- and y-directions, (d) $k_y = +n/\eta_2$, (e) $k_x = +\mathcal{P}/\eta_1$, and (f) 3D band structure for $\lambda_2 = -2\lambda_1 = 1.0$ eV along both x- and y-directions.

focus on these two only in the present paper. For the first case, we obtain

$$\mathcal{E}_X^{\mu,\nu}(\vec{k}) = \mu\sqrt{\tilde{f}(\vec{k}) + \nu\tilde{g}(\vec{k})}, \tag{5}$$

where $\tilde{f}(\vec{k}) = \mathcal{P}^2 + \left(\eta_1^2 + 4\lambda_1^2\right)k_x^2 + 4\,\lambda_1\left(\eta_1 - \eta_2\right)k_x\,k_y + \left(\eta_2^2 + 4\,\lambda_1^2\right)k_y^2$ and $\tilde{g}(\vec{k}) = 2\Big[\left(\mathcal{P}^2\,\eta_1^2 + 4\,n^2\,\lambda_1^2\right)k_x^2 + \left(n^2\,\eta_2^2 + 4\,\lambda_1^2\,\mathcal{P}^2\,k_y^2\right) + 4\,\lambda_1\left(\mathcal{P}^2\eta_1 - n^2\eta_2\right)k_x\,k_y\Big]^{1/2}$. As for the second case, we have the same relations by substituting $2\,\lambda_1 \mapsto \lambda_1$ only.

The band structure diagram of pristine surface Dirac fermions in SnTe (001) as well as in terms of these two different Rashba couplings $\lambda_2 = \lambda_1$ and $\lambda_2 = -2\lambda_1$ are plotted in Fig. 2. Also, we have considered four different momenta (a) $k_y = 0$, (b) $k_x = 0$, (c) $k_y = +nn/\eta_2$, and (d) $k_x = +\mathcal{P}/\eta_1$. When the RSOC is absent, i.e. $\lambda_2 = \lambda_1 = 0$ eV, energies $\mathcal{E} = \pm\mathcal{P}$ appear at $k_x = k_y = 0$, while at $\Lambda_x = (+\mathcal{P}/\eta_1, 0)$ and $\Lambda_x' = (-\mathcal{P}/\eta_1, 0)$, the Fermi surface is located at the energy $\mathcal{E} = 0$ eV [see solid black bands in Fig. 2(a)]. These two gapless points determine the metallic phase of SnTe (001) surface states. However, in the presence of RSOC, for the case of $\lambda_2 = \lambda_1 = 0.75$ eV, two new k_x points with a gapped phase emerge [see dashed blue bands in Fig. 2(a)]. Since the coordinates of these new points are not the same with the pristine Dirac points, one concludes that the Dirac cones are not in the same positions anymore and there is a change in the spatial distribution wave-packets. To this end, Fig. 2(c) shows that for $k_y = 0$, the Λ_x and Λ_x' points shown in Fig. 1 are not at the pristine k_x coordinates and the mirror symmetry is broken absolutely. This implies that the rotational band structure occurs, which is a characteristic fingerprint of the presence of RSOC. For this reason, the system is not gapless in the presence of RSOC and massive Dirac fermions on the SnTe (001) surface are responsible for the system dynamics, beneficial for the topological optoelectronics. This, in turn, alters the GV and EM of principle Dirac fermions, since the slope and concavity of all bands change, which will be discussed later in detail.

Physically point of view, the surface states projected by the bulk states need to introduce a new surface orientation for the topological Dirac cones because the Dirac cones are still there with new Cartesian coordinates and great potential is evident for a direction-dependent topological phase transition. Of course, the real strength of the RSOCs is important for such a report, which has yet to be reported. For stronger RSOCs, i.e. the case of $\lambda_2 = -2\lambda_1 = 1.0$ eV [see dotted red bands in Fig. 2(a)], smaller new k_x appear but the gap size is increased with RSOC, as expected from the dispersion energy relation Eq. (5). This can be understood from the different rotational band structure than the case of $\lambda_2 = \lambda_1 = 0.75$ eV, as demonstrated in Fig. 2(f). Also, as a result of this, different GV and EMs are expected to appear in these RSOCs compared to the previous same ones. We would like to stress that the high-energy Dirac-like points with energies $\mathcal{E} = \pm\mathcal{P}$ are not changed both energetically and locally. Thus, the RSOC affects the low-energy dynamics, not high-energy ones. As for the pure y-direction, in Fig. 2(b), two points $S_1 = (0, +n/\eta_2)$ and $S_2 = (0, -n/\eta_2)$ occurs at $k_x = 0$, which are those saddle points mentioned before, leading to the Lifshitz transition at energy $\mathcal{E} = \pm\delta$. When the RSOCs take the same signs and the same absolute values, i.e. the first competition, we see that the gap 2δ decreases at new $k_y < |S_{1/2}|$ points and the system remains in its initial gapped phase. As the RSOC strength increases, almost the same $S_{1/2}$ points appears, but Fig. 2(f) tells us that these points are not the previous saddle points, however; the same slopes and concavities along the y-direction as the saddle points emerge. It will be confirmed later using the GV and EM plots.

Let us focus on non-pure directions, i.e. when $k_y \neq 0$ ($k_x \neq 0$) along the x-direction (y-direction). As the main critical points for topological features of surface Dirac fermions in SnTe (001), we have set $k_y = +n/\eta_2$ and $k_x = +\mathcal{P}/\eta_1$, respectively. Two weak saddle points at $k_x = \pm\mathcal{P}/2\eta_1$ with energies $|\mathcal{E}| < \delta$ as well as one extremum at $k_x = 0$ with energies $|\mathcal{E}| = \delta$ are observed in the case of $\lambda_2 = \lambda_1 = 0$ eV, as shown in Fig. 2(d). As soon as the RSOC is turned on, one of the weak saddle points becomes stronger, resulting in mirror symmetry breaking. The gap between these new saddle points in the valence and conduction bands decreases with RSOC slightly. In this case, the slope and concavity of bands change drastically compared to the pure directions. Finally, the non-pure y-direction gives rise to a massless-to-massive Dirac fermion transition, as the gap opens with RSOC. However, as Fig. 2(e) shows, the Dirac cones are not located at the same positions, confirming Fig. 2(a), (c) and (f). Note that in both Fig. 2(d) and (e), the changes are shifted to the $k_x > 0$ and $k_y > 0$, because of the choices $k_y > 0$ and $k_x > 0$, respectively.

3. RSOC-induced group velocity

Bloch electronic waves describe clearly the basic properties of electronic transport properties of a condensed matter system [67,68]. If we consider wave vectors $\vec{k}$, the $\alpha \in \{x, y\}$ component of the momenta-dependent GV is the certain velocity of dispersive wave packets, given by

$$v_\alpha^{\mu,\nu}(\vec{k}) = \partial_{k_\alpha}\mathcal{E}_X^{\mu,\nu}(\vec{k}), \tag{6}$$

which is a first derivative of the dispersion energy concerning the α component of the momentum. From this relation, the real-space motion of the surface fermions in SnTe (001) can be easily obtained. Thus, by substituting the respective dispersion energy into Eq. (8) we obtain the GV components. However, we restrict ourselves to the pure directions to study the RSOC effects on the GV along the x- and y-direction. By this, for the case of $k_y = 0$ and $k_x = 0$, we obtain, respectively,

$$v_x^{\mu,\nu}(k_x) = \frac{k_x}{\mathcal{E}_X^{\mu,\nu}(k_x)}\left(4\lambda_1^2 + \eta_1^2 + \nu\frac{\sqrt{\mathcal{P}^2\eta_1^2 + 4\,n^2\,\lambda_1^2}}{k_x}\right), \tag{7a}$$

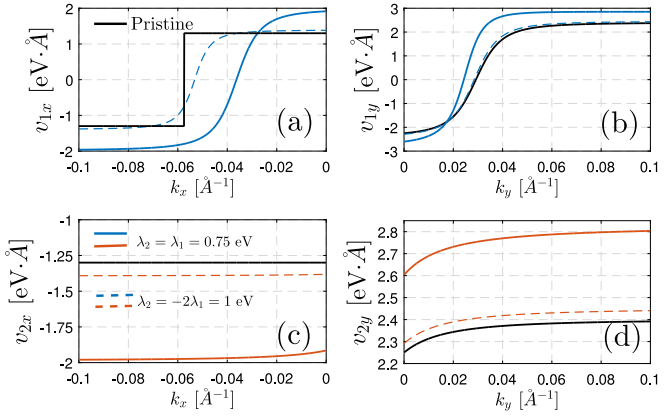

Fig. 3. (Color online) The RSOC-induced anisotropic group velocity of surface Dirac fermion in topological crystalline insulator SnTe (001) for {(a),(b)} lowest conduction band and {(c),(d)} highest conduction band.

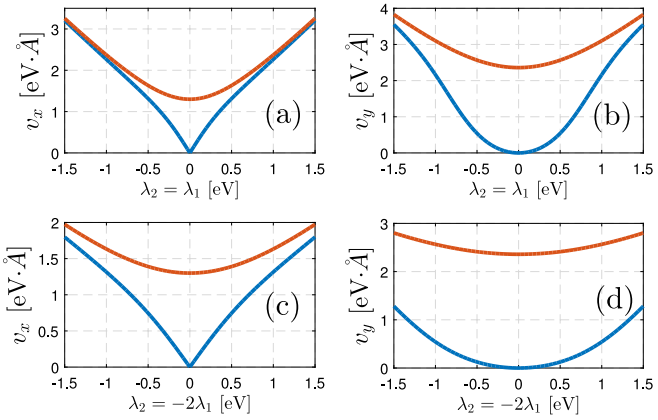

Fig. 4. (Color online) Anisotropic group velocity of surface Dirac fermion in topological crystalline insulator SnTe (001) as a function of RSOC for (upper panels) $\lambda_2 = \lambda_1$ at (a) $\{k_y = 0, k_x = +\mathcal{P}/\eta_1\}$ and (b) $\{k_x = 0, k_y = +n/\eta_2\}$ and for (lower panels) $\lambda_2 = -2\lambda_1$ at (c) $\{k_y = 0, k_x = +\mathcal{P}/\eta_1\}$ and (d) $\{k_x = 0, k_y = +n/\eta_2\}$.

$$v_y^{\mu,\nu}(k_y) = \frac{k_y}{\mathcal{E}_X^{\mu,\nu}(k_y)}\left(4\lambda_1^2 + \eta_2^2 + \nu\frac{\sqrt{4\,\mathcal{P}^2\lambda_1^2 + n^2\,\eta_2^2}}{k_y}\right), \tag{7b}$$

when $\lambda_2 = \lambda_1 = 0.75$ eV. The relations for the case of $\lambda_2 = -2\lambda_1$ are the same if one substitutes $2\,\lambda_1 \mapsto \lambda_1$ only. These orientation-dependent equations help us to confirm our claim on the anisotropic transport properties of SnTe (001) surface. Note that, at $k_x = 0$ and/or $k_y = 0$, the energy $\mathcal{E}_X^{\mu,\nu}(0,0)$ is equal to $\pm\mathcal{P}$ in the presence of RSOC [see Fig. 2(a) and (b)], and independent of the momentum. For this reason, $v_x^{\mu,\nu}(k_x,0)$ as well as $v_y^{\mu,\nu}(0,k_y)$ are not zero because of the second momentum-independent terms. However, for $k_y = +n/\eta_2$ and/or $k_x = +\mathcal{P}/\eta_1$, the energy $\mathcal{E}_X^{\mu,\nu}(0,0)$ is $\pm\delta$ and non-zero (depending on the competition between λ_1 and λ_2), respectively [see Fig. 2(d) and (e)].

We begin the analysis with some notes on the plots in the following. First, we will focus on the GV of two bands among four bands only, since there is symmetry between the valence and conduction bands. From this point, we divide the conduction band along the x-direction into two subbands, one dispersing from $\mathcal{E} = 0$ eV to $\mathcal{E} = +\mathcal{P}$ eV and another one for $\mathcal{E} > +\mathcal{P}$ eV. For the y-direction, we have two subbands as well dispersing from $\mathcal{E} = +\delta$ eV to $\mathcal{E} = +\mathcal{P}$ eV and $\mathcal{E} > +\mathcal{P}$ eV. Thereby, the blue $v_{1x/1y}$ and red $v_{2x/2y}$ curves in the following stand for the lowest and highest conduction subband, respectively.

In Fig. 3, we plot the orientation-dependent GV of Dirac fermions on the SnTe (001) surface in the absence and presence of RSOCs. It should be noted that the x-axis in all panels are half of the SBZ, i.e. $-0.1 \leq k_x \leq 0$ [Å^{-1}] and $0 \leq k_y \leq 0.1$ [Å^{-1}] in order to see clearly the changes of the conduction bands with the RSOC. In this figure, we consider two discussed RSOCs $\lambda_2 = \lambda_1 = 0.75$ eV as well as $\lambda_2 = -2\lambda_1 = 1.0$ eV only and will present a systematic study to cover all possible values of competitions $\lambda_2 = \lambda_1 \neq 0$ as well as $\lambda_2 \neq \lambda_1 \neq 0$ later. As mentioned already, we set two pure directions for the velocities including $k_y = 0$ and $k_x = 0$ in Fig. 3{(a),(c)} and {(b),(d)} for the lowest and highest conduction band, respectively. For $\lambda_2 = \lambda_1 = 0$ eV, we have the GV $v_x^{\nu}(k_x) = \eta_1\left(\eta_1\,k_x + \nu\mathcal{P}\right)/\mathcal{E}_X^{\nu}(k_x,0)$, leading to the black curves in panels {(a),(c)} for the x-direction. At $v_x = \pm\eta_1$, the Dirac fermions behave linearly with k_x and at $k_x = \pm\mathcal{P}/\eta_1$, it becomes zero. That can be understood from the slope of surface gapless bands in Fig. 2 as well. The negative and positive values of v_1x and v_2x refer to the direction of spatial distribution of waves originating from the slope up or down of the bands. However, once the RSOC is switched on with strengths $\lambda_2 = \lambda_1 = 0.75$ eV (the solid curves), the GVs decrease (increase) at non-zero (zero) k_x, since the system is gapped with the gap of 1.5δ [see dashed blue curves in Fig. 2(a)] and the slopes are far away from the pristine bands. It is clear that the high-energy GV v_{2x} should not change significantly, since the Dirac-like bands with energies $\pm\mathcal{P}$ are not changed with RSOC, neither at non-zero nor zero k_x. Thereby, a plateau for the case of $\lambda_2 = -2\lambda_1 = 1.0$ eV is expected as well for v_{2x}, while the gapped phase allows a stronger change for the v_{1x} [see dashed curves in Fig. 3{(a),(c)}]. As the dispersion energy bands say, the slopes at non-zero and zero k_x seem to be the same as the pristine case, leading to $v_{1x} \simeq \pm\eta_1$.

Now, we turn to the y-direction GVs v_{1y} and v_{2y}. For the case of $k_x = 0$, i.e. Fig. 3(b), we obtain $v_y^{\nu}(k_y) = \eta_2\left(\eta_2\,k_y + \nu n\right)/\mathcal{E}_X^{\nu}(k_y,0)$. The GV of pristine lower conduction band is zero at $k_y = +n/\eta_2 \simeq +0.03$ and opposite signs for v_{1y} is expected to emerge before and after this critical point, as confirmed in Fig. 3(b), however; for the upper conduction band [Fig. 3(d)] a positive or negative sign for v_{2y} appears with a slightly increasing trend with k_y. Note that we cannot say anything about the values of v_{2y} at the critical momentum $k_y = +n/\eta_2 \simeq +0.03$. However, after this point, the plot shows almost a plateau with the value of $\simeq +\eta_2$. That is also the case for the maximum value of v_{1y}. For the RSOC-induced velocities, i.e. blue and red curves in Fig. 3(b) and (d), v_{1y} indicates a smaller k_y for which it becomes zero with the opposite signs before and after that but with smaller and larger velocities, respectively, since the y-direction gap is decreased with $\lambda_2 = \lambda_1 = 0.75$ eV. The corresponding v_{2y} also illustrate a different value compared to the pristine case, but with the same slightly increasing trend and the same sign. As the last analysis for this figure, the case of $\lambda_2 = -2\lambda_1 = 1.0$ eV, as Fig. 2(b) says, both v_{1y} and v_{2y} should not show any big differences in comparison with the pristine SnTe (001) surface, as shown in red curves of Fig. 3(b) and (d).

Technically, the GVs as a systematic function of λ_1 and λ_2 at spacing of 0.01 across both $\lambda_2 = \lambda_1$ and $\lambda_2 = -2\lambda_1$. By this, we might as well get everything beyond what explained before for only two cases. This information will make the analysis much easier to construct the text. For the case of $k_y = 0.0$ and $k_x = +\mathcal{P}/\eta_1$, the GV versus $\lambda_2 = \lambda_1$ indicates a symmetric plot, as illustrated in Fig. 4(a). This stems from the mirror symmetry of the dispersing branches of the band structure at these coordinates. There are different behaviors for the conduction bands when the RSOCs are not strong enough, while they converge and become the same when RSOCs are strong. First of all, the zero and non-zero (η_1) values of GV of the lowest and highest conduction band, respectively, are observed at $\lambda_2 = \lambda_1 = 0$ eV. The GV of both bands decreases with $\lambda_2 = \lambda_1 < 0$, whereas it increases with $\lambda_2 = \lambda_1 > 0$. While from $|\lambda_2 = \lambda_1| = 1.5$ eV to 1 eV there is no difference between the slope of conduction bands, their slope becomes different from $|\lambda_2 = \lambda_1| = 1.0$ eV to 0 eV significantly. At $k_x = 0$ and $k_y = +n/\eta_2$, while v_y is zero for blue conduction band at $\lambda_2 = \lambda_1 = 0$ eV, it is equal to η_2 for the red conduction band at the same RSOCs, as shown in Fig. 4(b). In

contrast to the υ_x, both conduction bands show different slopes over the considered RSOC range. It is still a symmetric plot and shows a decreasing and increasing behavior for $\lambda_2 = \lambda_1 < 0$ and $\lambda_2 = \lambda_1 > 0$, respectively. From the curves of υ_x and υ_y, it is clear that GVs are anisotropic, which is the main message of the present work.

Let us turn to the second RSOCs configuration $\lambda_2 = -2\lambda_1$. At first glance, the GV values are reduced around one order of magnitude compared to the previous case, leading to a bigger difference between the GVs of lower and upper conduction bands, as represented in Fig. 4(c) and (d). The anisotropic behavior for both υ_x and υ_y can be seen. Also, the decreasing and increasing curves with $\lambda_2 = -2\lambda_1 < 0$ and $\lambda_2 = -2\lambda_1 > 0$ appear. Besides, neither in υ_x nor υ_y, there are no points for which the GVs are converged to the same values, in contrast to Fig. 4(a). It is important to note that at low RSOCs, near $k_x \neq 0$ and $k_y = 0$ as well as near $k_y \neq 0$ and $k_x = 0$, υ_x and υ_y are isotropic for both bands, coinciding with the η_1 and η_2, respectively. However, as we add non-zero larger RSOCs to the Dirac cones (moving away from the Dirac points), they are anisotropic. From these results, it is obvious that RSOCs and directions should be considered in the calculations of physical quantities since perturbation effects enhance these features. As a quick comparison with the Dirac cones in graphene and other 2D systems, one stress that these results do not appear when the Dirac theory is used only. By this, we mean that in the absence of intervalley scattering parameters n and δ and eventually $\mathcal{P}$, the same behaviors (but doubled) appear for SnTe (001) surface Dirac fermions.

4. RSOC-induced effective mass

Let us turn to another fundamental electronic transport property, EM. It is expected to have the same trends for both pristine and RSOC-induced EM as GV because the concavity of bands originates from the slope of the bands. Similar to GV plots, we will focus on the EM of two bands among four bands only as well with the same divided energies described before. Thus, the blue $m^*_{1x/1y}$ and red $m^*_{2x/2y}$ curves in the following stand for the lowest and highest conduction subband, respectively. Studying EM is useful to understand the fundamental electro-optical properties of materials, however, due to the long history of a mass in physics, there are many different EM definitions [69–72]. The mass term in an energy dispersion, leading to the band gap opening, is necessary for the valley-selective optical absorption to occur [73]. For the design and development of functional SnTe (001) surface-based devices, one needs to address the EM of Dirac fermions. In doing so, it is common to use an alternative definition, i.e. the second derivative of the energy dispersion, which is generally energy and momentum dependent. So, for the flavor $\alpha \in \{x, y\}$, the EM can be calculated straightforwardly

$$\frac{1}{m^{*\mu,\nu}_{\alpha}(\vec{k})} = \partial^2_{k_\alpha} \mathcal{E}^{\mu,\nu}_{X_1}(\vec{k}). \tag{8}$$

Using the implicit second derivative of the Eq. (5), simply, the following expressions can be derived for the pure x- and y-direction, respectively,

$$\begin{aligned}
&\frac{1}{m^{*\mu,\nu}_{x}(k_x)} = \\
&-\frac{k_x^2}{\left[\mathcal{E}^{\mu,\nu}_{X}(k_x)\right]^3}\left(\eta_1^2 + 4\lambda_1^2 - 2\nu\frac{\mathcal{P}^2\eta_1^2 + 4n^2\lambda_1^2}{g(k_x)}\right)^2 \\
&-\frac{1}{\mathcal{E}^{\mu,\nu}_{X}(k_x)}\left(\eta_1^2 + 4\lambda_1^2 + 8\nu\frac{k_y^2\left(\mathcal{P}^2\eta_1^2 + 4n^2\lambda_1^2\right)^2}{g^3(k_x)}\right) \\
&+\frac{1}{\mathcal{E}^{\mu,\nu}_{X}(k_x)}\left(2\nu\frac{\mathcal{P}^2\eta_1^2 + 4n^2\lambda_1^2}{g(k_x)}\right),
\end{aligned} \tag{9a}$$

$$\frac{1}{m^{*\mu,\nu}_{y}(k_y)} =$$

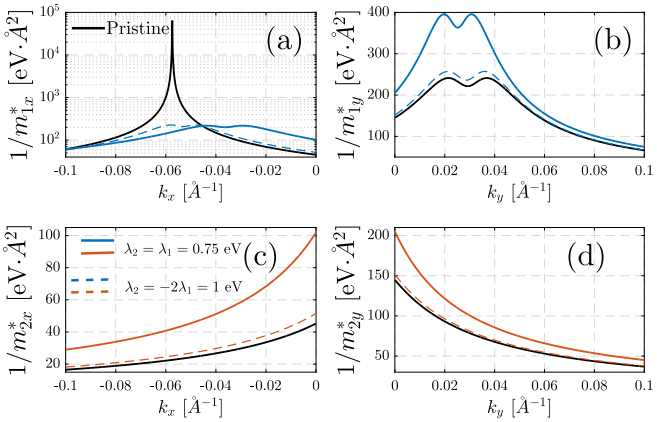

Fig. 5. (Color online) The RSOC-induced anisotropic effective mass of surface Dirac fermion in topological crystalline insulator SnTe (001) for {(a), (b)} lowest conduction band and {(c), (d)} highest conduction band.

$$\begin{aligned}
&-\frac{k_x^2}{\left[\mathcal{E}^{\mu,\nu}_{X}(k_y)\right]^3}\left(\eta_1^2 + 4\lambda_1^2 - 2\nu\frac{4\mathcal{P}^2\lambda_1^2 + n^2\eta_2^2}{g(k_y)}\right)^2 \\
&-\frac{1}{\mathcal{E}^{\mu,\nu}_{X}(k_y)}\left(\eta_1^2 + 4\lambda_1^2 + 8\nu\frac{k_y^2\left(4\mathcal{P}^2\lambda_1^2 + n^2\eta_2^2\right)^2}{g^3(k_y)}\right) \\
&+\frac{1}{\mathcal{E}^{\mu,\nu}_{X}(k_y)}\left(2\nu\frac{4\mathcal{P}^2\lambda_1^2 + n^2\eta_2^2}{g(k_y)}\right).
\end{aligned} \tag{9b}$$

Similarly, for the case of $\lambda_2 = -2\lambda_1$, by substituting $2\lambda_1 \mapsto \lambda_1$ in the above equations, one achieves the corresponding EM relations.

The highlight may be an increase or decrease of the EM with wave-vector or even the RSOC in the following. This is fundamentally related to the degeneracy of bands, implying that the curvature of energy bands characterizes the corresponding density of states. From the pristine bands of Fig. 1, it seems that the energy separation between band edges along the y-direction is considerably greater than the x-direction, meaning that the principal band edge effective mass along the x-direction is much smaller than the y-direction. This is confirmed in Fig. 5 for which $1/m^*_y \ll 1/m^*_x$ or $m^*_x \ll m^*_y$ independent of the momenta. This, in turn, means that the state associated with the heavy-mass band is related to the y-direction and the transport is faster along the x-direction. However, this is the case for the pristine surface and in the presence of RSOC, the value of m^*_x or m^*_y depends on the magnitude of the RSOC. As the GV calculations, we choose the most favorable configurations for λ_1 and λ_2. To estimate the role of RSOC, we have performed numerical calculations for two constant cases first. The resulting EMs are presented in Fig. 5.

Our results for (upper panels) the upper conduction band and (lower panels) the lower conduction band are shown in Fig. 5(a), (b), (c), and (d), respectively, for pure directions along the x- and y-direction. Similar to the GV, for $k_x = k_y = 0$ values, the EM of both conduction bands shows the same values and as expected EM along both directions are isotopic. Again, the maximum value of EM in panel (a), i.e. when $k_y = 0$, is taken place at $k_x = \pm\mathcal{P}/\eta_1$, whilst it is the case (on average) at $k_y = \pm n/\eta_2$ for EM in panel (b). Due to the curvature of the bands at these critical momenta, a minimum and maximum EF was expected clearly, as confirmed by the inverse of EMs in panels (a) and (b). The most dramatic signature of the upper conduction band, detectable in transport, is that the behavior near the neutrality point changes with a few orders of magnitude difference when the same RSOCs are considered, i.e. the solid blue and red curves. This means that the EM of both conduction bands decreases with RSOC. Following this decrease, the position of maximum EM is shifted forward or upward depending on the RSOC magnitude. This is valid for both directions. In contrast, the dashed curves correspond to the almost initial state

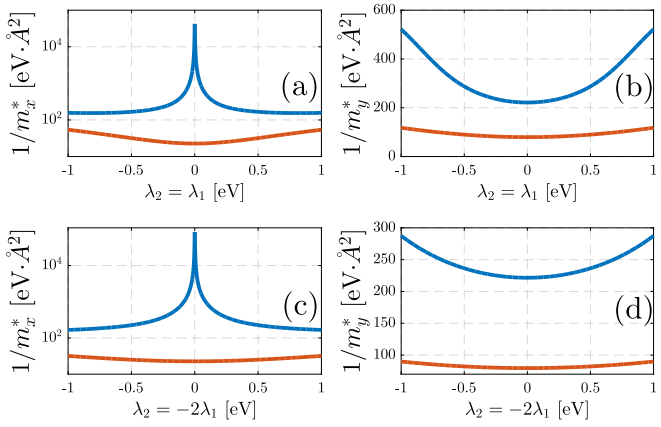

Fig. 6. (Color online) Anisotropic effective mass of surface Dirac fermions in topological crystalline insulator SnTe (001) as a function of RSOC for (upper panels) $\lambda_2 = \lambda_1$ at (a) $\{k_y = 0, k_x = +\mathcal{P}/\eta_1\}$ and (b) $\{k_x = 0, k_y = +n/\eta_2\}$ and for (lower panels) $\lambda_2 = -2\lambda_1$ at (c) $\{k_y = 0, k_x = +\mathcal{P}/\eta_1\}$ and (d) $\{k_x = 0, k_y = +n/\eta_2\}$.

of the Dirac fermions; different RSOC $\lambda_2 = -2\lambda_1 = 1.0$ eV leads to appearing the same curve near the pristine curve. We conjecture that the transport, in this case, remains metallic. The above-mentioned analysis is independent of the direction and for both EMs, they are valid. Nevertheless, these may change slightly or drastically when k_y or k_x is non-zero along each direction because of the dispersing bands presented in Fig. 2(c) and (d).

An important consequence of RSOC in the EM of spectrum Dirac fermions is studied systematically in Fig. 6. From the upper and lower panels, it is clear that the case of $\lambda_2 = \lambda_1$ as well as $\lambda_2 = -2\lambda_1$ of RSOCs do not change the qualitative behavior of the EM curves; its main effect is to make the difference between the EM of branches in the conduction band wider. This, in turn, means that there is a symmetry breaking of the gapless bands [see Fig. 2] down to a shift the gap boundaries. This is a direct consequence of oblique valleys associated with carriers in the band structure.

The detailed analysis performed for $1/m_x^*$ and $1/m_y^*$ as a function of RSOCs, whereby EM minima and maxima are identified is plotted in Fig. 6. Taking the zero RSOC at the plots, both $1/m_x^*$ and $1/m_y^*$ are expected to show the values corresponding to the black curves in Fig. 5, but since we are located at $k_x = +\mathcal{P}/\eta_1$ and $k_y = +n/\eta_2$, the EM along both directions is not isotropic. The EMs are mirror-symmetric with respect to RSOC sign independent of the upper or lower conduction band, evidencing that the SnTe (001) surface is tunable by the RSOC to construct the phase transition. While $1/m_x^*$ of the upper conduction bands increases with $\lambda_2 = \lambda_1 < 0$ as well as with $\lambda_2 = -2\lambda_1 < 0$ and decreases with their opposite sign, it happens for the lower conduction band vice versa. However, for $1/m_y^*$ this is not the case and both conduction bands decrease and increase, respectively, with $\{\lambda_2 = \lambda_1 < 0, \lambda_2 = -2\lambda_1 < 0\}$ and $\{\lambda_2 = \lambda_1 > 0, \lambda_2 = -2\lambda_1 > 0\}$. This can be another confirmation for the intrinsic anisotropic feature of SnTe (001) surface Dirac fermions.

5. Summary

Using the framework of the semi-classical $\vec{k} \cdot \vec{p}$ theory, we have addressed a question of how RSOC affects the fundamental surface topological physics of SnTe (001). Particularly, dispersion energy, GV and EM quantities are studied. The rotational band structures as a characteristic fingerprint of the RSOC-induced topological phase transition is observed. Regarding the RSOC magnitude, massless-to-massive Dirac fermion transition takes place at gapless states. We have shown that the RSOC modifies the critical values of direction-dependent GV and EM at which the transition occurs. Besides, we found out that the surface denotes the symmetric results for dispersion energy, GV and EM with RSOC sign independent of the direction. A possible application of our results can be anticipated in the field of optoelectronics using the TCI-based facilities.

Declaration of competing interest

The authors declare that they have no known competing financial interests or personal relationships that could have appeared to influence the work reported in this paper.

CRediT authorship contribution statement

Khang D. Pham: Conceptualization, Investigation, Formal analysis. **Nguyen T.T. Binh:** Conceptualization, Investigation, Formal analysis. **Ho Viet:** Software, Formal analysis, Writing - review & editing, Conceptualization. **Nguyen T. Dung:** Software, Formal analysis, Writing - review & editing, Conceptualization. **Bui D. Hoi:** Conceptualization, Methodology, Investigation, Formal analysis, Writing - review & editing.

References

[1] M.Z. Hasan, C.L. Kane, Rev. Modern Phys. 82 (2010) 3045.
[2] X.-L. Qi, S.-C. Zhang, Rev. Modern Phys. 83 (2011) 1057.
[3] A. Bansil, H. Lin, T. Das, Rev. Modern Phys. 88 (2016) 021004.
[4] L. Fu, C.L. Kane, E.J. Mele, Phys. Rev. Lett. 98 (2007) 106803.
[5] D.J. Thouless, M. Kohmoto, M.P. Nightingale, M. den Nijs, Phys. Rev. Lett. 49 (1982) 405.
[6] S.-Y. Xu, Y. Xia, L.A. Wray, S. Jia, F. Meier, J.H. Dil, J. Osterwalder, B. Slomski, A. Bansil, H. Lin, R.J. Cava, M.Z. Hasan, Science 332 (2011) 560.
[7] M. Brahlek, N. Bansal, N. Koirala, S.-Y. Xu, M. Neupane, C. Liu, M.Z. Hasan, S. Oh, Phys. Rev. Lett. 109 (2012) 186403.
[8] S.-Y. Xu, C. Liu, N. Alidoust, M. Neupane, D. Qian, I. Belopolski, J.D. Denlinger, Y.J. Wang, H. Lin, L.A. Wray, G. Landolt, B. Slomski, J.H. Dil, A. Marcinkova, E. Morosan, Q. Gibson, R. Sankar, F.C. Chou, R.J. Cava, A. Bansil, M.Z. Hasan, Nature Commun. 3 (2012) 2191.
[9] J. Zhang, W.-X. Ji, C.-W. Zhang, P. Li, P.-J. Wang, Phys. Chem. Chem. Phys. 20 (2018) 24790.
[10] R.-W. Zhang, C.-W. Zhang, W.-X. Ji, S.-S. Li, S.-J. Hu, S.-S. Yan, P. Li, P.-J. Wang, F. Li, New J. Phys. 17 (2015) 083036.
[11] M. Yarmohammadi, Phys. Lett. A 380 (48) (2016) 4062.
[12] B.D. Hoi, M. Yarmohammadi, J. Magn. Magn. Mater. 454 (2018) 362.
[13] K.S. Novoselov, et al., Science 306 (5696) (2004) 666.
[14] M. Yarmohammadi, Chin. Phys. B 26 (2) (2017) 026502.
[15] A.H.C. Neto, F. Guinea, N.M.R. Peres, K.S. Novoselov, A.K. Geim, Rev. Modern Phys. 81 (1) (2009) 109.
[16] K.S. Novoselov, et al., Nature 438 (7065) (2005) 197.
[17] M. Yarmohammadi, J. Magn. Magn. Mater. 426 (2017) 621.
[18] M. Yarmohammadi, Phys. Lett. A 381 (14) (2017) 1261.
[19] M. Ezawa, Phys. Rev. Lett. 109 (5) (2012) 055502.
[20] M. Ezawa, New J. Phys. 14 (3) (2012) 033003.
[21] M. Yarmohammadi, RSC Adv. 7 (18) (2017) 10650.
[22] M. Yarmohammadi, Solid State Commun. 250 (2017) 84.
[23] L. Fu, Phys. Rev. Lett. 106 (2011) 106802.
[24] A.P. Schnyder, S. Ryu, A. Furusaki, A.W.W. Ludwig, Phys. Rev. B 78 (2008) 195125.
[25] A. Kitaev, AIP Conf. Proc. 1134 (2009) 22.
[26] Y. Ando, L. Fu, Annu. Rev. Condens. Matter Phys. 6 (2015) 361.
[27] T.H. Hsieh, H. Lin, J. Liu, W. Duan, A. Bansil, L. Fu, Nature Commun. 3 (2012) 982.
[28] P. Dziawa, B.J. Kowalski, K. Dybko, R. Buczko, A. Szczerbakow, M. Szot, E. usakowska, T. Balasubramanian, B.M. Wojek, M.H. Berntsen, O. Tjernberg, T. Story, Nature Mater. 11 (2012) 1023.
[29] Y. Tanaka, Z. Ren, T. Sato, K. Nakayama, S. Souma, T. Takahashi, K. Segawa, Y. Ando, Nat. Phys. 8 (2012) 800.
[30] S.-Y. Xu, C. Liu, N. Alidoust, M. Neupane, D. Qian, I. Belopolski, J. Denlinger, Y. Wang, H. Lin, L. Wray, G. Landolt, B. Slomski, J. Dil, A. Marcinkova, E. Morosan, Q. Gibson, R. Sankar, F. Chou, R. Cava, A. Bansil, M. Hasan, Nature Commun. 3 (2012) 1192.
[31] J.C.Y. Teo, L. Fu, C.L. Kane, Phys. Rev. B 78 (2008) 045426.
[32] P. Barone, D. Di Sante, S. Picozzi, Phys. Status Solidi RRL 7 (2013) 1102.
[33] L. Zhao, J. Wang, B.-L. Gu, W. Duan, Phys. Rev. B 91 (2015) 195320.
[34] Y. Tanaka, T. Sato, K. Nakayama, S. Souma, T. Takahashi, et al., Phys. Rev. B 87 (2015) 155105.
[35] M. Serbyn, L. Fu, Phys. Rev. B 90 (2014) 035402.

[36] E. Tang, L. Fu, Nat. Phys. 10 (2014) 964.
[37] J. Liu, T.H. Hsieh, P. Wei, W. Duan, J. Moodera, et al., Nature Mater. 13 (2014) 178.
[38] X. Qian, L. Fu, J. Li, Nano Res. 8 (2015) 967.
[39] L. Fu, C.L. Kane, Phys. Rev. Lett. 109 (2012) 246605.
[40] H. Imamura, P. Bruno, Y. Utsumi, Phys. Rev. B 69 (2004) 121303(R).
[41] D.A. Abanin, D.A. Pesin, Phys. Rev. Lett. 106 (2011) 136802.
[42] M. Shiranzaei, H. Cheraghchi, F. Parhizgar, Phys. Rev. B 96 (2017) 024413.
[43] M. Ezawa, Phys. Rev. Lett. 121 (2018) 116801.
[44] M. Ezawa, New J. Phys. 16 (2014) 065015.
[45] J. Nitta, T. Akazaki, H. Takayanagi, T. Enoki, Phys. Rev. Lett. 78 (1997) 1335.
[46] G. Engels, J. Lange, T. Schäpers, H. Lüth, Phys. Rev. B 55 (1997) R1958.
[47] D. Grundler, Phys. Rev. Lett. 84 (2000) 6074.
[48] T. Koga, J. Nitta, T. Akazaki, H. Takayanagi, Phys. Rev. Lett. 89 (2002) 046801.
[49] J. Liu, W. Duan, L. Fu, Phys. Rev. B 88 (2013) 241303(R).
[50] R.-J. Slager, A. Mesaros, V. Juricic, J. Zaanen, Nat. Phys. 9 (2012) 98.
[51] C.-K. Chiu, H. Yao, S. Ryu, Phys. Rev. B 88 (2013) 075142.
[52] T. Morimoto, A. Furusaki, Phys. Rev. B 88 (2013) 125129.
[53] P. Jadaun, D. Xiao, Q. Niu, S.K. Banerjee, Phys. Rev. B 88 (2013) 085110.
[54] W.A. Benalcazar, J.C.Y. Teo, T.L. Hughes, Phys. Rev. B 89 (2014) 224503.
[55] C. Fang, L. Fu, Phys. Rev. B 91 (2015) 161105(R).
[56] M. Diez, D.I. Pikulin, I.C. Fulga, J. Tworzydło, New J. Phys. 17 (2015) 043014.
[57] M. Kargarian, G.A. Fiete, Phys. Rev. Lett. 110 (2013) 156403.
[58] E.O. Wrasse, T.M. Schmidt, Nano Lett. 14 (2014) 5717.
[59] X. Zhou, C.-H. Hsu, T.-R. Chang, H.-J. Tien, Q. Ma, P.J. Herrero, N. Gedik, A. Bansil, V.M. Pereira, S.-Y. Xu, H. Lin, L. Fu, Phys. Rev. B 98 (2018) 241104(R).
[60] T. Morimoto, A. Furusaki, C. Mudry, Phys. Rev. B 91 (2015) 235111.
[61] Y. Tanaka, T. Shoman, K. Nakayama, S. Souma, T. Sato, T. Takahashi, M. Novak, K. Segawa, Y. Ando, Phys. Rev. B 88 (2013) 235126.
[62] C.M. Polley, P. Dziawa, A. Reszka, A. Szczerbakow, R. Minikayev, J.Z. Domagala, S. Safaei, P. Kacman, R. Buczko, J. Adell, M.H. Berntsen, B.M. Wojek, O. Tjernberg, B.J. Kowalski, T. Story, T. Balasubramanian, Phys. Rev. B 89 (2014) 075317.
[63] Y. Okada, M. Serbyn, H. Lin, D. Walkup, W. Zhou, et al., Science 341 (2013) 1496.
[64] D. Bercioux, P. Lucignano, Rep. Progr. Phys. 78 (2015) 106001.
[65] M. Yarmohammadi, K. Mirabbaszadeh, Phys. Chem. Chem. Phys. 21 (2019) 21633.
[66] M. Yarmohammadi, K. Mirabbaszadeh, J. Mater. Chem. A 7 (2019) 25573.
[67] G.D. Mahan, Many Particle Physics, Plenum Press, New York, 1993.
[68] G. Grosso, G.P. Parravicini, Solid State Physics, Academic Press, New York, 2014.
[69] N.W. Aschcroft, Solid State Theory, Holt, Rinehart, and Wilson, 1976.
[70] K. Seeger, Semiconductor Physics, Springer-Verlag, 1985.
[71] C. Kittel, Introduction to Solid State Physics, second ed., Wiley, 1986.
[72] W.A. Harrison, Solid State Theory, Dover, 1979.
[73] M. Ezawa, Phys. Rev. B 89 (2014) 195413.